ACS OMEGA

http://pubs.acs.org/journal/acsodf

Article

Synthesis and Characterization of Ultrathin $FeTe_2$ Nanocrystals

Dana Capitano,* Zhixiang Hu, Yu Liu, Xiao Tong, Dmytro Nykypanchuk, Donald DiMarzio, and Cedomir Petrovic*

Cite This: *ACS Omega* 2021, 6, 10537−10546

Read Online

ACCESS | Metrics & More | Article Recommendations

ABSTRACT: Ultrathin crystals including monolayers have been reported for various transition-metal dichalcogenides (TMDCs) with van der Waals bonds in the crystal structure. Herein, we report a detailed synthesis procedure and characterization of ultrathin iron ditelluride crystals. This material crystallizes in an orthorhombic marcasite *Pnnm* crystal structure whose bonding is dominantly covalent and without loosely connected van der Waals (vdW) bonds, making monolayer $FeTe_2$ synthesis less straightforward than other TMDC monolayer syntheses. The chemical vapor deposition synthesis process described is simple, effective, and results in a range of crystal thicknesses from approximately 400 nm down to the $FeTe_2$ monolayer.

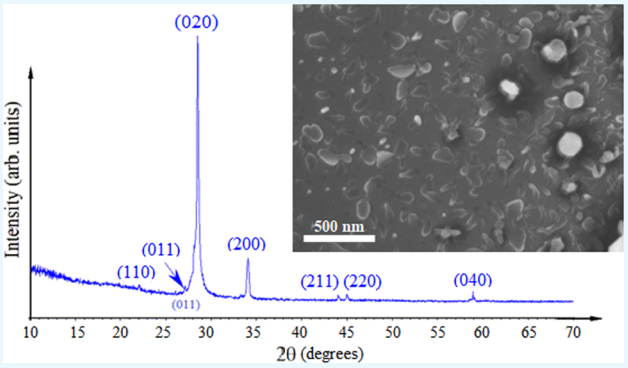

INTRODUCTION

Iron ditelluride ($FeTe_2$) is one of the several transition-metal dichalcogenide crystals first synthesized and observed by Steffan Tengner in 1938.[1] $FeTe_2$ is known to form in either marcasite-type or pyrite-type crystals, depending on the synthesis conditions. The orthorhombic marcasite structure is the more common crystal phase formed under ambient conditions, while the cubic pyrite phase is formed through high-temperature and high-pressure synthesis techniques.[2]

Marcasite $FeTe_2$ adopts either a *Pnnm*[1,3] or *Pnn*2-type[4] orthorhombic unit cell, where Fe is octahedrally coordinated by Te. Density functional theory found no significant energy difference between the two arrangements.[5] Early studies show that $FeTe_2$ crystals have an anisotropic antiferromagnetic ground state below about 80 K and a possible ferromagnetic (FM) state below approximately 30 K.[6−8] The electronic structure features a reported band gap of 0.35−0.67 eV, as deduced from electrical transport measurements.[7,9] $FeTe_2$ thin films have been found to feature a low thermal conductivity value of 1.20 W m^{-1} K^{-1}.[10] Electron-doped marcasite $FeTe_2$ crystals are a good candidate for thermoelectric applications due to the sharp increase in density of states around the band edges, which favors a large increase in the thermoelectric power factor $S^2\sigma$, where S is the thermopower and σ is the electrical conductivity.[5]

$FeTe_2$ nanoparticles have previously been synthesized using solution-based methods, where all reactions take place between 120 and 300 °C. Low-temperature hydrothermal synthesis produced 25 nm diameter spherical nanoparticles[11] and nanorods[12] that can be indexed to orthorhombic $FeTe_2$. FM $FeTe_2$ nanocrystallites[13] were also prepared using a hydrothermal method. Hot-injection solvothermal methods under atmospheres of inert gasses like nitrogen and argon have produced $FeTe_2$ nanorods,[14] a colloidal solution of $FeTe_2$ nanocrystals,[15] and magnetic spherical $FeTe_2$ crystallites that aggregate into treelike architectures.[16] Irregular $FeTe_2$ nanocrystallites[13,16] with dimensions on the order of several hundred nanometers were found to be ferromagnetic at room temperature. These solutions utilize relatively mild temperatures and deliver crystals of variable morphologies. However, they are also relatively time-consuming, require complicated precursor solution syntheses prior to the $FeTe_2$ formation reaction, and necessarily involve filtration, washing, and drying/resuspension steps. These steps not only add extensive hands-on involvement but can also be a source of contamination.

The development of a more facile synthesis method for $FeTe_2$ nanocrystals is of high interest, particularly methods that can produce relatively clean materials for future studies. It has been known for some time that nanocrystals with vdW bonds in the crystal structure, such as TMDCs, can be produced using chemical vapor deposition methods.[17−21] The synthesis of ultrathin TMDC nanocrystals has enabled many important discoveries.[22−24]

Received: October 5, 2020
Accepted: February 12, 2021
Published: April 12, 2021

Since neither marcasite nor pyrite crystals are vdW solids, monolayer $FeTe_2$ was formerly considered nonexistent.[25] This conclusion was reasonable, as it can be seen in Figure 1 that

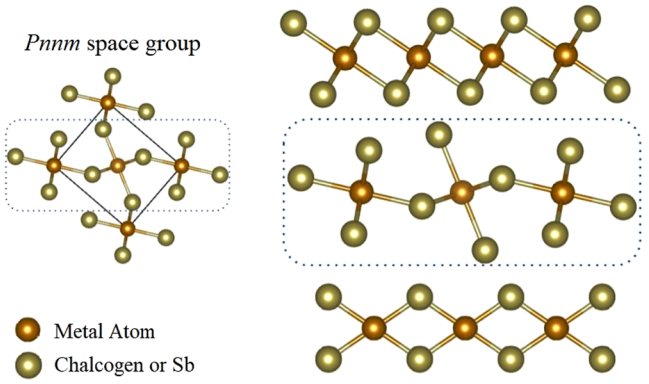

Figure 1. Comparison of marcasite *Pnnm* space group with the 1T (*P*31*m*, CdI_2-type) and 2H (*P*63/*mmc*, NbS_2-type) crystal structures of transition-metal dichalcogenides. Note the absence of van der Waals bonds in the marcasite crystal structure.

neither the 1T nor 2H atomic layer structures common in TMDCs are directly derived from the *Pnnm* space group crystal unit cell. However, multiple first-principles studies, where monolayer $FeTe_2$ was studied,[5,26−29] concluded that it is possible for this material to be energetically stable in monolayer form in ambient conditions based on calculated phonon-dispersion frequencies. When both the octahedral (T) and trigonal-prismatic (H) coordinations of Fe were compared, it was found that the H phase had lower energy than the T phase,[2] making it the more thermodynamically favorable of the two. As a result, most first-principles calculations of monolayer $FeTe_2$ consider the H phase.

The magnetic state of monolayer $FeTe_2$ is predicted to be either FM or ferromagnetic with calculated moment values in the range from 1.08 to 2 μ_B.[5,28,29] Magnetocrystalline anisotropy (MCA) that favors the in-plane direction[28] and the MCA dependence on an applied electric field for multiple MTe_2 compound monolayers[27] were predicted. The $FeTe_2$ easy axis flips from in-plane to out-of-plane as the applied electric field increases, giving monolayer $FeTe_2$ excellent potential for applications in magnetic memory devices. Magnetic anisotropy has also been noted in experiments on bulk $FeTe_2$ crystals.[7]

There is some debate about the electronic character of the $FeTe_2$ monolayer. Two studies found it to exhibit semiconducting behavior, with band gaps of and 0.87[2] and 0.35 eV,[5] which are on the order of those observed in TMDCs. However, other studies found $FeTe_2$ monolayer to exhibit metallic behavior[25,26,28] and half-metallicity,[27,29] making it a potential candidate for applications in spintronics as spin valves. Gudelli et al.[5] also found in their first-principle theoretical study of the thermoelectric properties of monolayer $FeSe_2$ and $FeTe_2$ that marcasite $FeTe_2$ is a good thermoelectric material that favors electron doping. Its hole and electron concentrations were calculated to be 9.2×10^{19} and 1.4×10^{21} cm^{-3} for the thermopower values of 96 and −74 mV K^{-1} at 300 and 600 K, respectively. $FeTe_2$ also had calculated relaxation times of 2.3×10^{-14} and 3.1×10^{-14} s at those respective temperatures.

It is clear that $FeTe_2$ is a material with promising qualities for future applications that remains relatively unstudied experimentally. With the lack of efficient large-scale syntheses of this material being an obstruction of progress in this field, it is vital to further develop its nanomaterial production methods. In this work, we present a chemical vapor deposition process to synthesize $FeTe_2$ nanocrystals of various sizes down to monolayer thickness. This more facile process allows for nanocrystal synthesis directly on the substrate from simple powder precursors in a relatively short interval of time. Crystal structure and unit cell parameters of deposited nanostructures were investigated through X-ray diffraction. A scanning electron microscope (SEM) was used to obtain images confirming nanoparticle deposition, lateral sizes, and morphologies. The energy-dispersive X-ray spectroscopy (EDS) capability of the SEM was used to determine the chemical composition of nanostructures within the sample. Raman spectroscopy also confirmed that $FeTe_2$ phase crystals formed in this experiment. Atomic force microscopy (AFM) data was used to calculate and compare the lateral and vertical size dimensions of deposited nanostructures.

RESULTS

X-ray Diffraction and Energy-Dispersive Spectroscopy. Figure 2 shows the X-ray diffraction scan of the substrate

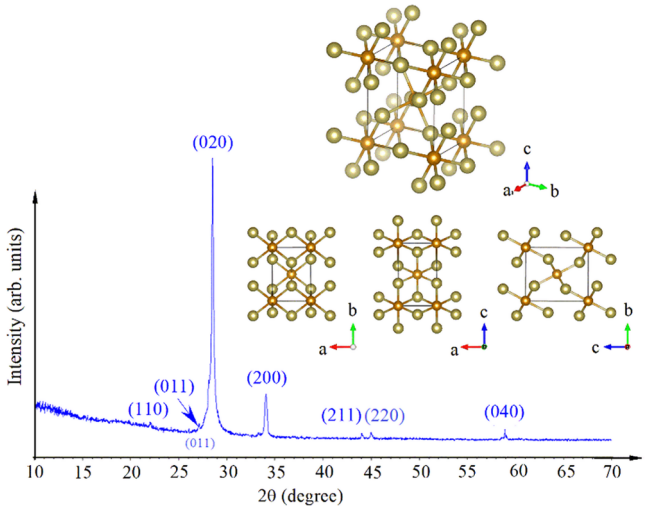

Figure 2. X-ray diffraction pattern for deposited $FeTe_2$ crystals. The inset shows the $FeTe_2$ crystal structure.

after deposition. All diffraction peaks can be indexed in the orthorhombic *Pnnm* (58) space group, with the calculated lattice parameters $a = 5.262(2)$ Å, $b = 6.2608(2)$ Å, and $c = 3.871(2)$ Å. These values correspond well to the reported standard values[10,13] with no impurity present.

Diffraction peaks can be seen at 28.49° (020) and 34.01° (200), and weak peaks at 22.05° (110), 27.11° (011), 44.00° (211), 44.98° (220), and 58.92° (040). The strongest peak is at 28.49° (020), and the peak for its parallel plane (040) is visible as well. Due to the orthorhombic lattice structure of this crystal, the (200) plane is also symmetrical to the (020) and (040) planes. The symmetry of the two largest peaks indicates the preferential orientation of crystals on the substrate with their {0*k*0} faces aligned to the substrate direction, or faces of the type {200} or {100}. The presence of peaks for the (110) and (220) planes, which are symmetrical, as well as the (211) and (011) planes, indicate that although there is preferential orientation along the (010) plane, the deposits have a certain range of preferred crystallization.

https://doi.org/10.1021/acsomega.0c04872
ACS Omega 2021, 6, 10537−10546

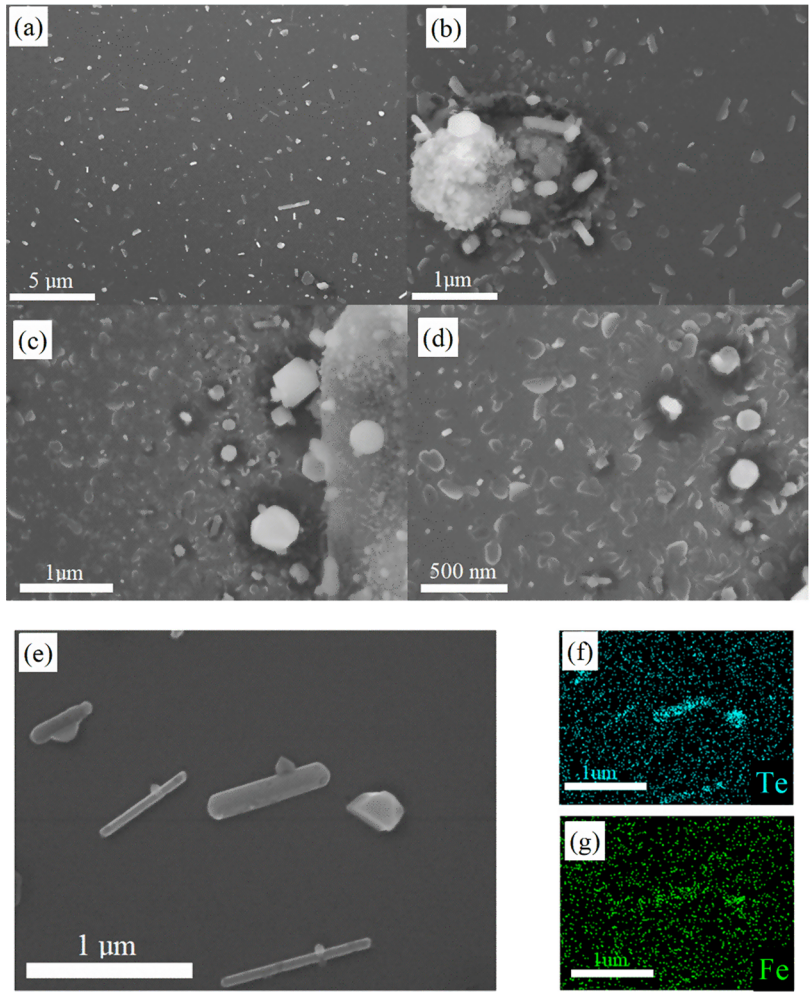

Figure 3. (a–e) Scanning electron microscope images at various magnifications of the as-synthesized $FeTe_2$ nanocrystals. (f, g) Elemental mapping of target nanocrystals for tellurium (f) and iron (g) concentrations.

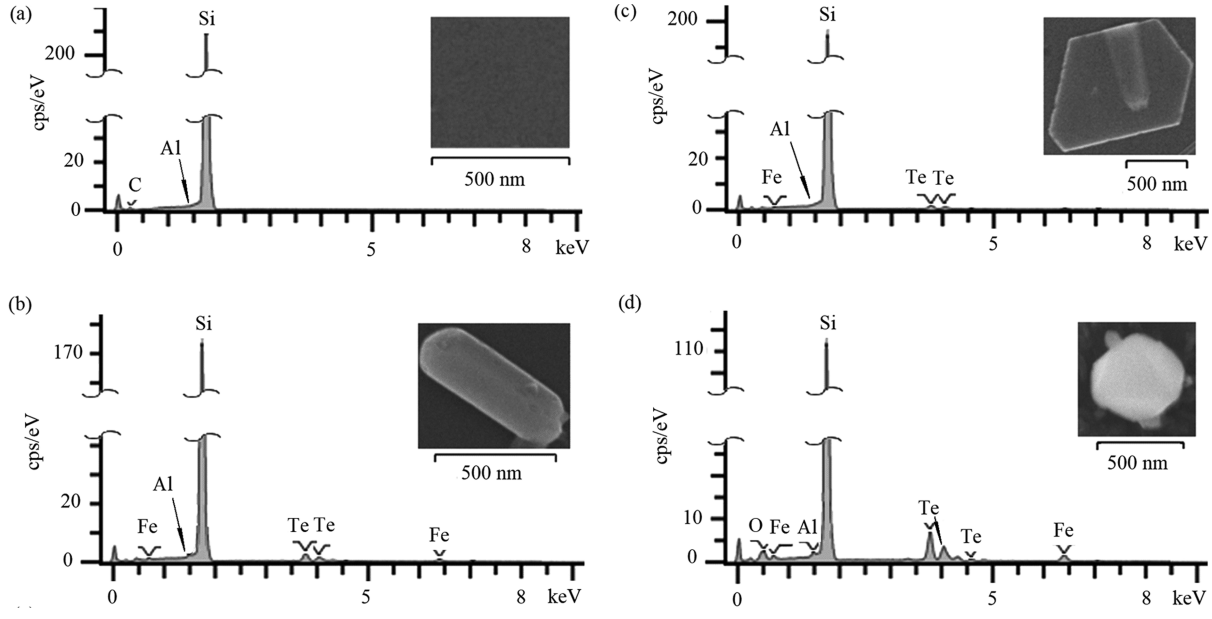

Figure 4. Energy-dispersive X-ray spectroscopy spectra taken on a substrate before deposition (a) and on selected crystals (b–d).

Scanning Electron Microscopy. Figure 3a–e consists of several medium- and high-magnification SEM images of the crystallized deposition products on the substrate. As can be seen in the medium-magnification image (a), the chemical vapor

https://doi.org/10.1021/acsomega.0c04872
ACS Omega 2021, 6, 10537−10546

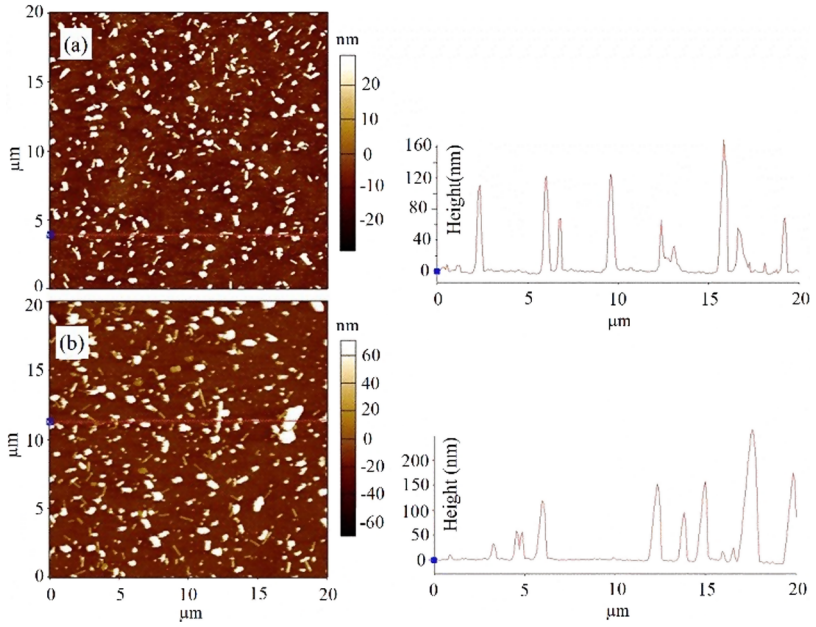

Figure 5. Atomic force microscope images at two different areas (a, b) with scan sizes of 20 μm with line scans corresponding to the horizontal red lines across each image.

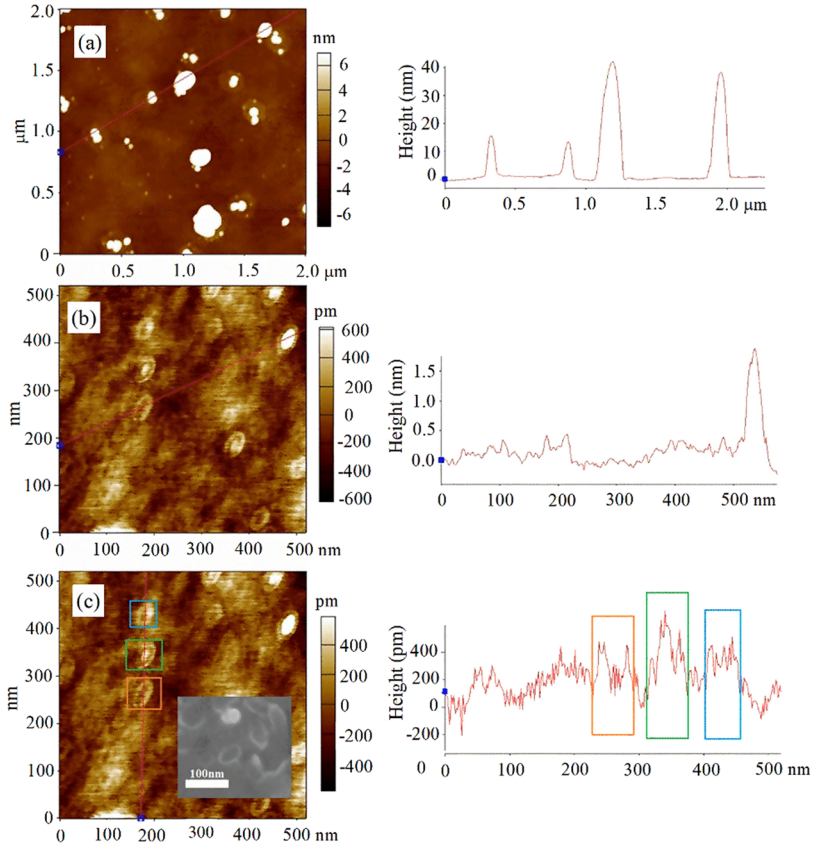

Figure 6. Atomic force microscope images with scan sizes of (a) 2.0 μm and (b, c) 500 nm and their accompanying line scans. (c) Boxes to designate the borders of each scanned nanoplate and an inset that shows a proportionate scanning electron microscope image of nanoplates for comparison.

deposition process delivers results with a high dispersibility and nanostructures that range in size and morphology. The nanoparticles produced in this reaction can be separated into three classes based on the order of their largest lateral dimension: those with dimensions greater than 1 μm, those with dimensions between 100 nm and 1 μm, and those with all lateral dimensions less than 100 nm.

Crystal morphology was not found to be size-dependent, with multiple configurations present throughout the sample. The most common structure, seen in Figure 3a,b, consists of oblong plates with rounded edges. These elongated oval or rectangular

https://doi.org/10.1021/acsomega.0c04872
ACS Omega 2021, 6, 10537−10546

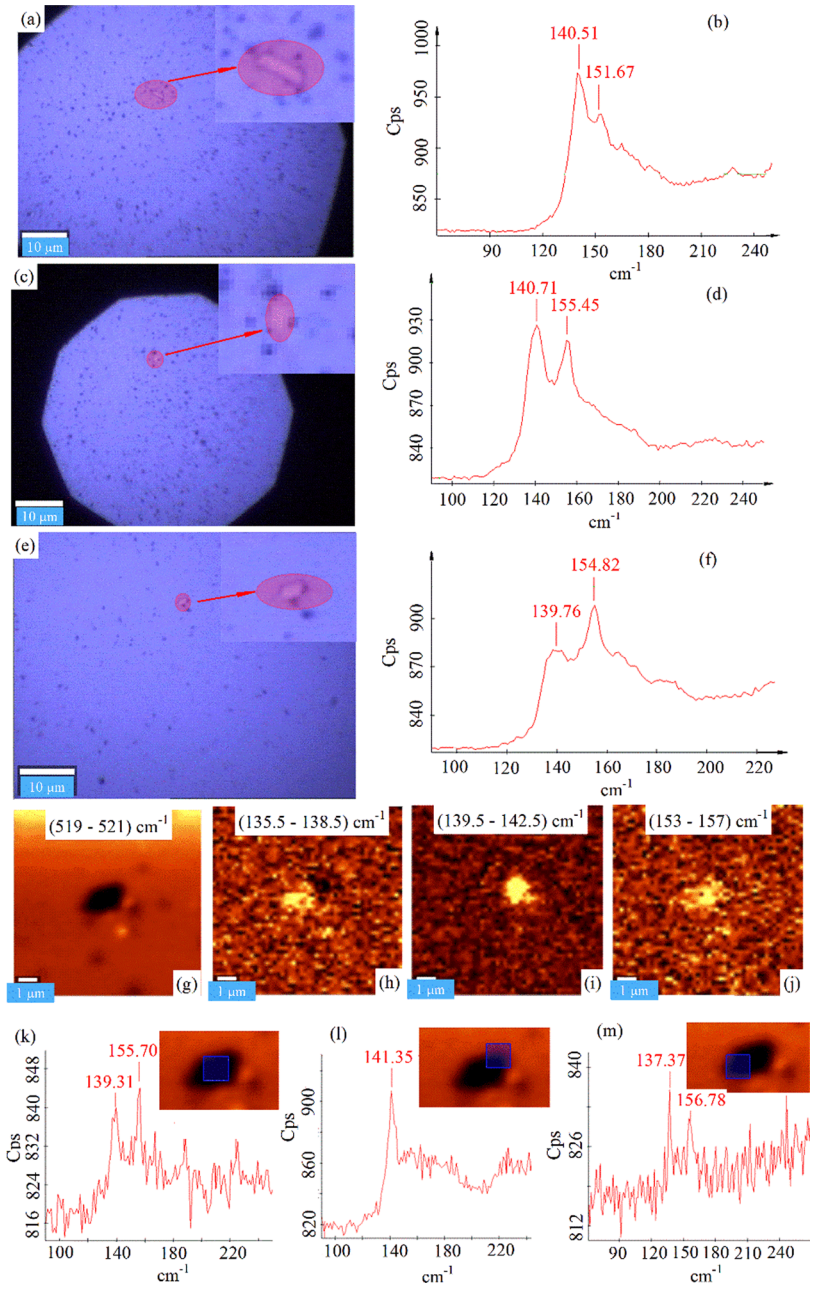

Figure 7. Raman peaks of $FeTe_2$ nanoplates with lateral dimensions above 1 μm of oblong (a, b) and two different rounded shapes (c–f). (g) Two-dimensional mapping at 520.7 cm^{-1} Si crystalline Raman peak. Since $FeTe_2$ nanoplates block the Si Raman signal, the shape and dimension of the dark feature in the mapping are used to identify the nanocrystal. (h–j) Raman intensity peak mapping for the crystal (e). Position dependence of Raman peaks of $FeTe_2$ (k–m); scale identical to (g).

structures are seen across all size ranges, with their length being their largest dimension. A less common morphology, visible in the bottom right corner of Figure 3a,c, is that of the elongated hexagonal particle, which is often darker in color than the oblong structures.

More common than the hexagonal particles are structures like those seen in Figure 3c, where deposits form from the clusters of smaller oblong and spherical particles. The spherical crystallites that make up the deposit in Figure 3c can also be seen individually in Figure 3d. Their lateral dimensions are all less than 100 nm, but their relative brightness indicates a significant thickness. The morphology that makes up the majority of the deposited particles in Figure 3d consists of oblong nanoplates with irregular edges. These also have lateral dimensions in the tens and hundreds of nanometers, but their dimness indicates a relatively lower vertical dimension. Most deposited structures have one elongated dimension. Elemental mapping (Figure 3f–g) done through energy-dispersive X-ray spectroscopy (EDS) confirms that deposited nanostructures are composed of both iron and tellurium.

The ratio of iron (Fe) to tellurium (Te) in structures of different sizes and morphologies as observed through EDS can be seen in Figure 4. The oblong structures (Figure 4b) have a Fe/Te ratio of 1:2, whereas deposits in (c) and (d) show the width of formation with Fe/Te ratio of 1:1.81 and 1:2.16, respectively. This indicates that different morphologies may result from minor fluctuations in molar ratio. Based on these observations and those from the diffractogram in Figure 2,

https://doi.org/10.1021/acsomega.0c04872
ACS Omega 2021, 6, 10537−10546

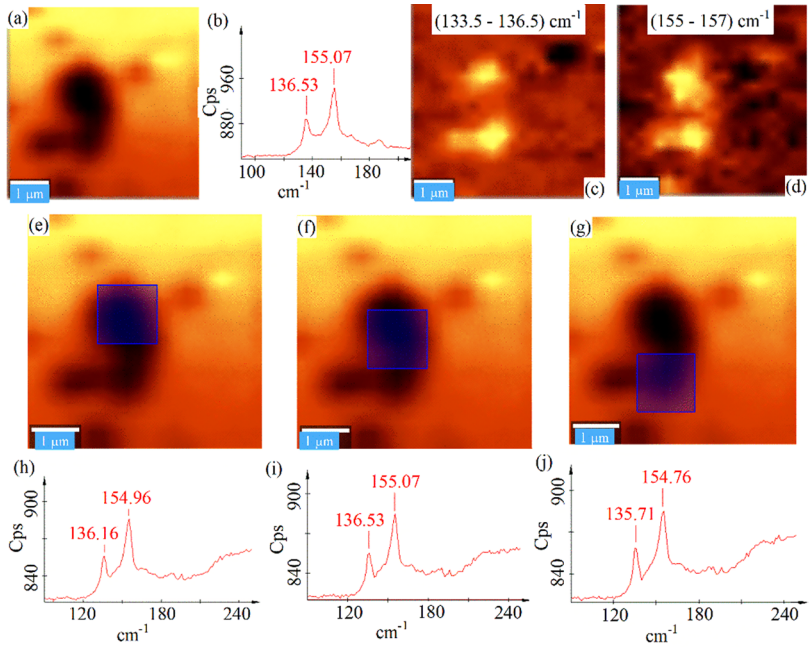

Figure 8. (a) Two-dimensional mapping at 520 cm^{-1} of Si crystalline Raman peak, analogous to Figure 7g. (b) Raman peaks, (c, d) Raman intensity, and (e−j) position peak mapping of oblong $FeTe_2$ nanoplates with lateral dimensions below 1 μm.

synthesized nanocrystals exhibit the orthorhombic marcasite $FeTe_2$ crystal structure. The deviation from ideal stoichiometry could arise from the interference with the silicon substrate, which could generate a stronger signal than the relatively thin deposited nanoparticles. The relatively high percentages of oxygen seen only in Figure 4d could be an evidence of oxidation and may indicate size-based air instability.

Atomic Force Microscopy. Figure 5 shows topographic atomic force microscopy images of the substrate surface with varying scan sizes. Each scan captures information about the vertical dimensions of the different size classes of deposited nanostructures. Images in Figure 5a,b, with scan sizes of 20 μm, confirm the high dispersibility of the nanostructures as seen through SEM. Their line scans show the vertical dimensions of features crossed by the matching line across the image. Nanocrystals with a dimension greater than 1 μm were found to have vertical dimensions ranging from 100 to 250 nm, and even up to 400 nm (not shown). Nanoparticles in the class with maximum lateral dimensions equal to or less than 1 μm have thicknesses ranging from 10 to 150 nm.

The nanocrystals measured in Figure 6 are significantly smaller, with lateral dimensions under 250 nm. Those measured in Figure 6a can be compared to the bright, round particles seen clustered together in Figure 6c. These particles have maximum lateral dimensions between 88 and 214 nm, and thicknesses in the range of 12−50 nm. For all particles discussed thus far, their height ranged between 10 and 33% of their largest lateral dimension. However, the particles in Figure 6b were found to have a significantly reduced height to length ratio.

The particles in Figure 6b appear to be the flat, irregularly shaped $FeTe_2$ nanoplates seen in Figure 3d. These crystals are in the lowest size range of those observed for both the SEM and AFM, and these images are directly compared in Figure 6c. These particles have smaller lateral dimensions than those in Figure 5a, with lengths measured between 43 and 62 nm. Their vertical dimensions are significantly lower, with thicknesses between approximately 400 pm and 2 nm, or between 0.5 and 3% of their lateral dimensions. These measurements are on the order of the lattice parameters found when analyzing the sample diffraction pattern, with the smallest lattice parameter measuring 386 pm. This indicates that the nanocrystals in Figure 6b,c are single to quadruple molecular layers of $FeTe_2$ unit cells.

Raman Spectroscopy. Raman peaks for bulk $FeTe_2$ crystals were previously reported at 119 and 137 cm^{-1} at room temperature.[7] A 154 cm^{-1} peak was also observed at low temperature,[7] and at room temperature in a different study.[30] The first two peaks are attributed to the B_{1g} mode associated with antiphase Te−Te vibration, whereas the 154 cm^{-1} mode is associated with A_{1g} in-phase mixed Te−Te stretching related to mutual Fe−Te motion within $FeTe_6$ octahedron and is sensitive to changes in bond lengths.[7,30] Raman spectra in this work (Figures 7 and 8) support the X-ray diffraction and energy-dispersive X-ray conclusion that $FeTe_2$ phase crystals were formed in this experiment.

We note that the elongated, oblonglike nanocrystals of several micron size show somewhat lower A_{1g} frequency and somewhat higher B_{1g} frequency when compared to bulk crystals (Figure 7a,b). In contrast, both frequencies are slightly increased in the rounded crystals (Figure 7c−f) of about 1 μm size. Interestingly, peak intensity mapping of one such round-shape nanoplate (Figure 7g−j) reveals that the broad B_{1g} mode (Figure 7f) splits into weak intensity bulk crystal like 137 cm^{-1} and strong intensity ~141 cm^{-1} vibration, whereas the weak A_{1g} mode shows a small shift to higher frequencies compared to bulk crystal. The selected spot Raman spectroscopy suggests that the A_{1g} mode tends to diminish near the crystal edge (Figure 7k−m).

Both B_{1g} (136 cm^{-1}) and A_{1g} (155 cm^{-1}) modes were observed in nanoplate crystals with lateral dimensions below 1 μm (Figure 8a,b), confirming the synthesis of submicron $FeTe_2$ nanoplates. Both modes are more intense near submicron crystal edges (Figure 8c,d), even though position mapping indicates the presence of both peaks along the crystallite length (Figure 8e−j). This could suggest that the $FeTe_2$ nanoplate growth mechanism

https://doi.org/10.1021/acsomega.0c04872
ACS Omega 2021, 6, 10537−10546

involves the reaction of Fe vapor from sublimed $FeCl_2$ (Scheme 1) with Te powder particle of several hundred micron sizes,

Scheme 1. Schematic Diagram for $FeTe_2$ Chemical Vapor Deposition Synthesis

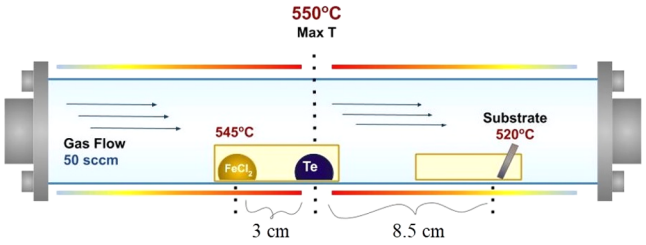

where $FeTe_2$ growth is facilitated along the lateral edges of Te powder. As nanoplates grow to micron (Figure 7e−m) and oblong rodlike shapes of several micron lateral lengths (Figure 7a−d), small Raman peak shifts imply changes in Fe−Te and Te−Te bond lengths in mesoscale $FeTe_2$.

The bond lengths and coordination numbers of surface atoms and bulk atoms are usually different; therefore, a shift in Raman frequencies could arise due to competing influences of surface atom undercoordination and bond-length changes. The undercoordination of surface atoms has a great impact on their vibrational frequency.[31,32] The above argument can be applied to the subtle changes of Raman peak shift seen due to the variety in size and shape among the nanoplates and between nanoplates and bulk. In particular, the atoms in crystal corners are usually undercoordinated when compared to the atoms in bulk and surface. Hence, the change in coordination number in the corners of nanoplates may influence the Fe−Te motion mode in Figure 7i,j. The peaks for the Te−Te mode are still observed at the corners, suggesting that the corners of the $FeTe_2$ plates are mainly terminated by Te atoms. The $FeTe_2$ plates in Figure 8 show a higher peak intensity mode of A_{1g} Fe−Te motion compared to the B_{1g} Te−Te mode.

The corner or edge effects are more obvious in smaller plates or elongated, oblonglike nanocrystals, so the peak intensity of the Te−Te mode is relatively higher than that of the Fe−Te mode, as shown in Figure 7a,b. For both single-selected spot Raman spectroscopy and 2D mapping over the surface areas of $FeTe_2$ plates, both Fe−Te motion (~151 cm^{-1}) and Te−Te mode (~137−140 cm^{-1}) peaks are observed and comparable, suggesting elementary stoichiometric structure in the $FeTe_2$ nanoplates.

DISCUSSION

$FeTe_2$ nanocrystals are of high interest for application in the new generation of hybrid energy storage devices such as lithium−ion capacitors and sodium−ion batteries that feature high power and energy density and a good cycle retention rate.[33,34] Further experiments on in situ chemical vapor deposition of $FeTe_2$ ultrathin crystals in porous carbon network are therefore of high interest. Moreover, since $FeTe_2$ monolayers are predicted to preserve a ferromagnetic state due to magnetocrystalline anisotropy arising from spin-orbit coupling,[28] further magneto-optic experiments are of interest to test theoretical predictions. Two-dimensional materials with ferromagnetic ground states attract great interest as they are possible candidates for spintronic and memory devices but can also be valuable in fundamental science studies.[35−37] Finally, since reproducible switching behavior without crystal structure changes has recently been reported in $FeTe_2$ nanostructures,[38] it would be of interest to investigate the size dependence of switching properties in future devices made from $FeTe_2$ ultrathin crystals.

CONCLUSIONS

In this experiment, $FeTe_2$ nanocrystallites of varying sizes and thicknesses down to the monolayer were grown using a facile chemical vapor deposition process. The deposited nanoparticles showed a high dispersibility and lateral dimensions ranging from less than 100 nm to above a micrometer. The most common crystal morphology is that of an oblong nanoplate with rounded edges. The observed nanocrystallites have stoichiometries corresponding to $FeTe_{2.0(2)}$. The X-ray diffractogram of this sample can be indexed to that of orthorhombic marcasite $FeTe_2$ with a *Pnnm* space group and no crystalline impurity phase present. The preferential orientation of deposited nanocrystals along the (010) plane is indicated by differences in relative peak intensities. Synthesized nanocrystallites have thicknesses ranging from picometers to 200 nm or between 0.5 and 33% of their largest lateral dimension. This indicates that the chemical vapor deposition process in this work is effective at synthesizing nanocrystalline $FeTe_2$ with disparate thicknesses down to the monolayer level on one substrate. Comparison of shape- and size-dependent Raman spectra suggests that $FeTe_2$ crystallites grow from the reaction of sublimed Fe on Te submicron particles on lateral edges. Future work of interest includes studies of chemical defects that could influence magnetic properties, chemical stability, and protection of dangling covalent bonds as well as size-dependent studies of magnetism in reduced dimensions using optical methods.

EXPERIMENTAL SECTION

Materials and Equipment. Anhydrous iron(II) chloride ($FeCl_2$) powder (99.5% Alfa Aesar) and Tellurium (Te) powder (99.99% Alfa Aesar) were used as chemical precursors for the synthesis of $FeTe_2$. Metal chloride powder precursors are preferable to their pure metal counterparts due to significantly increased vapor pressures at lower temperatures. For example, $FeCl_2$ has a vapor pressure of 0.1 mmHg at 490 °C and 1 mmHg at 570 °C,[39] whereas pure iron requires a temperature of 1412.5 °C to reach a vapor pressure of 0.1 mmHg.[40] Tellurium, however, has a vapor pressure of 1 mmHg at the relatively low temperature of 520 °C[39] and therefore can be used in pure form. The deposition substrates used were silicon thermal oxide wafers with a 285 nm silicon oxide layer (MTI Corporation), with lateral dimensions of 5 mm and a thickness of 0.5 mm. The precursors and substrate were placed in rectangular alumina crucibles of varying dimensions. The synthesis was performed inside a horizontal single-zone tubular furnace with a heating chamber 1 in. in diameter and 12 in. in length. A quartz process tube was used to contain the process. Experiments were done under a constant gas flow of 3% H_2 in Ar.

Synthetic Procedures. There are multiple crystalline phases of iron telluride that form based on synthesis temperature and precursor stoichiometry.[3,41] The marcasite structured ε-phase has been reported to have a homogeneity range from 66.1 to 67.4% tellurium and an accepted peritectic formation temperature of 649 °C.[41−43] The ε-$FeTe_2$ also forms from a eutectoid reaction at temperatures ranging from 514 to 517 °C.[42]

https://doi.org/10.1021/acsomega.0c04872
ACS Omega 2021, 6, 10537−10546

Scheme 1 presents the experimental setup for the chemical vapor deposition of $FeTe_2$. $FeCl_2$ and Te powders were obtained and used without further purification. They were placed in a single alumina crucible with a molar ratio of 1 mole $FeCl_2$/3 moles Te. The powder precursor masses were separated from each other by 3 cm to control their respective temperatures during the reaction. The crucible was placed in the furnace with the Te directly above the heating element and the $FeCl_2$ powder 3 cm upstream. Placing the $FeCl_2$ at a greater distance from the deposition substrate was done to lower the ratio of iron that reached the substrate compared to tellurium and to induce a 1:2 deposition stoichiometry on the substrate.

The substrate was removed from a sealed plastic sleeve and placed vertically at an angle inside a smaller crucible, with its polished face directed upstream. This crucible was placed, so the substrate was 8.5 cm downstream from the heating element. Crucible placement was designed to induce temperatures of 545, 550, and 520 °C on the $FeCl_2$, Te, and substrate, respectively, based on the measured temperature gradient using an external thermocouple since the result of synthesis is sensitive to the temperature of precursors and substrate. These temperatures were chosen based on precursor vaporization rates and the formation temperature for $FeTe_2$. The ends of the furnace's quartz tube were then closed, and the chamber flushed with 3% hydrogen balance argon carrier gas for 10 min prior to the start of the chemical vapor deposition reaction.

The chemical vapor deposition was performed under a constant carrier gas flow rate of 50 cubic centimeters per minute. The furnace was heated to a peak temperature of 550 °C from room temperature over 15 min at a rate of about 35 °C min^{-1}. This temperature was maintained for 30 min to induce precursor vaporization and deposition on the substrate, as well as the nucleation and growth of $FeTe_2$ crystals. After 30 min, the furnace was shut off and the system cooled under a constant gas flow. The furnace cooled naturally from 550 to 170 °C, at which point the furnace casing was opened for more rapid cooling. The substrates were removed from the furnace once it reached room temperature and placed in a glovebox to prevent oxidation. This entire process was completed over the course of approximately 4 h.

Characterization Methods. X-ray diffraction data was obtained using a Rigaku Miniflex with Cu Kα (λ = 0.15418 nm) radiation. The obtained diffraction pattern was analyzed using Rietica software. Scanning electron microscopy and energy-dispersive X-ray spectroscopy data were obtained using a JEOL JSM-7600F scanning electron microscope.

An Asylum Research MFP 3D operated using noncontact AC Air topography mode was used to take atomic force microscopy images and measure the surface topology of the sample. No sample treatment was necessary prior to the measurement for this experiment.

Raman experiments for single-selected point Raman spectrum acquisition and 2D Raman spectral imaging were performed using a WITec confocal Raman microscope alpha 300 equipped with a solid-state laser (λ = 532 nm), an electron multiplying CCD detector, and a 100×/0.9NA objective lens. Unpolarized Raman scattered light was focused onto a multimode fiber and monochromator with an 1800 line/mm grating. Instrument calibration was verified by checking the position of Si at 520.7 cm^{-1}.

AUTHOR INFORMATION

Corresponding Authors

Dana Capitano − *Condensed Matter Physics and Materials Science Department, Brookhaven National Laboratory, Upton, New York 11973, United States; Department of Materials Science and Chemical Engineering, Stony Brook University, Stony Brook, New York 11790, United States;* orcid.org/0000-0003-4848-6460; Email: danaacapitano@gmail.com

Cedomir Petrovic − *Condensed Matter Physics and Materials Science Department, Brookhaven National Laboratory, Upton, New York 11973, United States; Department of Materials Science and Chemical Engineering, Stony Brook University, Stony Brook, New York 11790, United States;* orcid.org/0000-0001-6063-1881; Email: petrovic@bnl.gov

Authors

Zhixiang Hu − *Condensed Matter Physics and Materials Science Department, Brookhaven National Laboratory, Upton, New York 11973, United States; Department of Materials Science and Chemical Engineering, Stony Brook University, Stony Brook, New York 11790, United States*

Yu Liu − *Condensed Matter Physics and Materials Science Department, Brookhaven National Laboratory, Upton, New York 11973, United States;* orcid.org/0000-0001-8886-2876

Xiao Tong − *Center for Functional Nanomaterials, Brookhaven National Laboratory, Upton, New York 11973, United States*

Dmytro Nykypanchuk − *Center for Functional Nanomaterials, Brookhaven National Laboratory, Upton, New York 11973, United States*

Donald DiMarzio − *Northrop Grumman Corporation, Redondo Beach, California 90278, United States*

Complete contact information is available at: https://pubs.acs.org/10.1021/acsomega.0c04872

Notes

The authors declare no competing financial interest.

ACKNOWLEDGMENTS

This work was supported by the US DOE Basic Energy Sciences, Materials Sciences and Engineering Division under Contract No. DE-SC0012704. Research carried out, in part, at the Centre for Functional Nanomaterials, Brookhaven National Laboratory, which is supported by the US Department of Energy, Office of Basic Energy Sciences, under Contract No. DE-SC0012704.

ABBREVIATIONS

TMDC, transition-metal dichalcogenide; vdW, van der Waals; Fe, iron; Te, tellurium; FM, ferromagnetic; MCA, magneto-crystalline anisotropy; MTe_2, metal ditelluride; $FeSe_2$, iron diselenide; H_2, hydrogen; $FeCl_2$, iron(II) chloride; EDS, energy-dispersive X-ray spectroscopy; SEM, scanning electron microscope; AFM, atomic force microscopy

REFERENCES

(1) Tengner, S. Über Diselenide und Ditelluride von Eisen, Kobalt und Nickel Diselenides. *Z. Anorg. Allg. Chem.* **1938**, *239*, 126−132.

(2) Ghosh, A.; Thangavel, R. Electronic structure and optical properties of iron based chalcogenide FeX_2 (X = S, Se, Te) for photovoltaic applications: a first principle study. *Indian J. Phys.* **2017**, *91*, 1339−1344.

https://doi.org/10.1021/acsomega.0c04872
ACS Omega 2021, 6, 10537−10546

(3) Grønvold, F.; Haraldsen, H.; Vihovde, J.; et al. Phase and Structural Relations in the system Iron Tellurium. *Acta Chem. Scand.* **1954**, *8*, 1927−1942.
(4) Brostigen, G.; Kjekshus, A.; et al. Compounds with the Marcasite Type Crystal Structure: V*. The Crystal Structure of FeS_2, $FeTe_2$, and $CoTe_2$. *Acta Chem. Scand.* **1970**, *24*, 1925−1940.
(5) Gudelli, V. K.; Kanchana, V.; Vaiheeswaran, G.; Valsakumarc, M. C.; Mahanti, S. D. Thermoelectric properties of marcasite and pyrite FeX_2 (X = Se, Te): a first principle study. *RSC Adv.* **2014**, 9424−9431.
(6) Finlayson, D. M.; Llewyellyn, J. P.; Smith, T. The Magnetic Susceptibility of Iron Ditelluride: II. *Proc. Phys. Soc.* **1959**, *74*, 75−80.
(7) Rahman, A.; Zhang, D.; Rehman, M. U.; Zhang, M.; Wang, X.; Dai, R.; Wang, Z.; Tao, X.; Zhang, Z. Multiple magnetic phase transitions, electrical and optical properties of $FeTe_2$ single crystals. *J. Phys.: Condens. Matter* **2019**, *32*, No. 035808.
(8) Xie, Y.; Zhu, L.; Jiang, X.; Lu, J.; Zheng, X.; He, W.; Li, Y. Mild Hydrothermal-Reduction Synthesis and Mössbauer Study of Low-Dimensional Iron Chalcogenide Microcrystals and Single Crystals. *Chem. Mater.* **2001**, *13*, 3927−3932.
(9) Parthasarathy, G.; Sharma, D. K.; Sharma, Y. K.; Chandra, U. High Pressure Electrical Resistivity Studies on $FeSe_2$ a,d $FeTe_2$. *AIP Conf. Proc.* **2013**, *1512*, 40.
(10) Mami, A.; Ben Messaoud, K.; Kamoun, O.; Malouk, M. Synthesis, physical study and efficient photocatalytic activity of $FeTe_2$. *J. Mater. Sci.: Mater. Electron.* **2019**, *30*, 6050−6058.
(11) Zhang, W.; Cheng, Y.; Zhan, J.; Yu, W.; Yang, L.; Chen, L.; Qian, Y. Synthesis of nanocrystalline marcasite iron ditelluride $FeTe_2$ in aqueous solution. *Mater. Sci. Eng., B* **2001**, *79*, 244−246.
(12) Zhang, W.; Yang, Z.; Zhan, J.; Yang, L.; Yu, W.; Zhou, G.; Qian, Y. Hydrothermal synthesis of marcasite iron ditelluride $FeTe_2$ nanorods at low temperature. *Mater. Lett.* **2001**, *47*, 367−370.
(13) Liu, A.; Chen, X.; Zhang, Z.; Jiang, Y.; Shi, C. Selective synthesis and magnetic properties of $FeSe_2$ and $FeTe_2$ nanocrystallites obtained through a hydrothermal co-reduction route. *Solid State Commun.* **2006**, *138*, 538−541.
(14) Oyler, K. D.; Ke, X.; Sines, I. T.; Schiffer, P.; Schaak, R. Chemical Synthesis of Two-Dimensional Iron Chalcogenide Nanosheets: FeSe, FeTe, Fe(Se,Te), and $FeTe_2$. *Chem. Mater.* **2009**, *21*, 3655−3661.
(15) Bastola, E.; Bhandari, K.; Matthews, A. J.; Shreshta, N.; Ellingson, R. J. Elemental anion thermal injection synthesis of nanocrystalline marcasite iron dichalcogenide $FeSe_2$ and $FeTe_2$. *RSC Adv.* **2016**, *6*, 69708−69714.
(16) Wang, H.; Wu, M.; Wang, Y.; Wang, H.; Huang, X.; Yang, X. Phosphine-free synthesis of $FeTe_2$ nanoparticles and self-assembly into tree-like nanoarchitectures. *Chin. Phys. B* **2019**, *28*, No. 106401.
(17) Tang, L.; Li, T.; Luo, Y.; Feng, S.; Cai, Z.; Zhang, H.; Liu, B.; Cheng, H. M. Vertical Chemical Vapor Deposition Growth of Highly Uniform 2D Transition Metal Dichalcogenides. *ACS Nano* **2020**, *14*, 4646−4653.
(18) Li, J.; Zhao, B.; Chen, P.; Wu, R.; Li, B.; Xia, Q.; Guo, G.; Luo, J.; Zang, K.; Zhang, Z.; Ma, H.; Sun, G.; Duan, X.; Duan, X. Synthesis of Ultrathin Metallic MTe_2 (M = V, Nb, Ta) Single-Crystalline Nanoplates. *Adv. Mater.* **2018**, *30*, No. 1801043.
(19) Lv, R.; Robinson, J. A.; Schaak, R. E.; Sun, D.; Sun, Y.; Mallouk, T. E.; Terrones, M. Transition metal dichalcogenides and beyond: synthesis, properties, and applications of single- and few-layer nanosheets. *Acc. Chem. Res.* **2015**, *48*, 56−64.
(20) Wang, X.; Gong, Y.; Shi, G.; Chow, W. L.; Keyshar, K.; Ye, G.; Vajtai, R.; Lou, J.; Liu, Z.; Ringe, E.; Tay, B. K.; Ajayan, P. M. Chemical vapor deposition growth of crystalline monolayer $MoSe_2$. *ACS Nano* **2014**, 5125−5131.
(21) Ma, H.; Chen, P.; Li, B.; Li, J.; Ai, R.; Zhang, Z.; Sun, G.; Yao, K.; Lin, Z.; Zhao, B.; Wu, R.; Tang, X.; Duan, X.; Duan, X. Synthesis of $WS_{2x}Se_{2-2x}$ Alloy Nanosheets with Composition-Tunable Electronic Properties. *Nano Lett.* **2018**, *18*, 3523−3529.
(22) Bonilla, M.; Kolekar, S.; Ma, Y.; Diaz, H. C.; Kalappattil, V.; Das, R.; Eggers, T.; Gutierrez, H. R.; Phan, M.; Batzill, M. Strong room-temperature ferromagnetism in VSe_2 monolayers on van der Waals substrates. *Nat. Nanotechnol.* **2018**, *13*, 289−293.
(23) Neumann, A.; Lindlau, J.; Colombier, L.; Nutz, M.; Najmaei, S.; Lou, J.; Mohite, A. D.; Yamaguchi, H.; Högele, A. Opto-valleytronic imaging of atomically thin semiconductors. *Nat. Nanotechnol.* **2017**, *12*, 329−335.
(24) Aivazian, G.; Gong, Z.; Jones, A. M.; Chu, R.-L.; Yan, J.; Mandrus, D. G.; Zhang, C.; Cobden, D.; Yao, W.; Xu, X. Magnetic control of valley pseudospin in monolayer WSe_2. *Nat. Phys.* **2015**, *11*, 148−152.
(25) Lan, M.; Xiang, G.; Nie, Y.; Yang, D.; Zhang, X. The static and dynamic magnetic properties of monolayer iron dioxide and iron dichalcogenides. *RSC Adv.* **2016**, *6*, 31758−31761.
(26) Ataca, C.; Sahin, H.; Circaci, S. Stable, Single-Layer MX_2 Transition-Metal Oxides and Dichalcogenides in a Honeycomb-Like Structure. *J. Phys. Chem. C* **2012**, *116*, 8983−8999.
(27) Sui, X.; Hu, T.; Wang, J.; Gu, B.; Duan, W.; Miao, M. Voltage-controllable colossal magnetocrystalline anisotropy in single-layer transition metal dichalcogenides. *Phys. Rev. B* **2017**, *96*, No. 041410.
(28) Chen, W.; Zhang, J.; Nie, Y.; Xia, Q.; Guo, G. Electronic structure and magnetism of MTe_2 (M = Ti, V, Cr, Mn, Fe, Co and Ni) monolayers. *J. Magn. Magn. Mater.* **2020**, *508*, No. 166878.
(29) Aras, M.; Kılıç, Ç.; Ciraci, S. Magnetic ground state in $FeTe_2$, VS_2, and $NiTe_2$ monolayers: Antiparallel magnetic moments at chalcogen atoms. *Phys. Rev. B* **2020**, *101*, No. 054429.
(30) Lutz, H. D.; Müller, B. Lattice Vibration Spectra. LXVIII. Single-Crystal Raman Spectra of Marcasite-type Iron Chalcogenides and Pnictides, FeX_2 (X = S, Se, Te; P, As, Sb). *Phys. Chem. Miner.* **1991**, *18*, 265−268.
(31) Gao, Y.; Zhao, X.; Yin, P.; Gao, F. Size-Dependent Raman Shifts for nanocrystals. *Sci. Rep.* **2016**, *6*, No. 20539.
(32) Li, H.; He, X. W.; Xiao, H. J.; Du, H. N.; Wang, J.; Zhang, H. X. Size-dependent Raman shift of semiconductor nanomaterials determined using bond number and strength. *Phys. Chem. Chem. Phys.* **2017**, *19*, 28056−28062.
(33) Jia, Q.-C.; Zhang, H.-J.; Kong, L.-B. Nanostructure-modified in-situ synthesis of nitrogen-doped porous carbon microspheres (NPCM) loaded with $FeTe_2$ nanocrystals and NPCM as superior anodes to construct high-performance lithium-ion capacitors. *Electrochim. Acta* **2020**, *337*, No. 135749.
(34) Cho, J. S.; Lee, S. Y.; Kang, Y. C.; et al. Iron Telluride-Decorated Reduced Graphene Oxide Hybrid Microspheres as Anode Materials with Improved Na-Ion Storage Properties. *ACS Appl. Mater. Interfaces* **2016**, *8*, 21343−21349.
(35) Gong, C.; Zhang, X. Two-dimensional magnetic crystals and emergent heterostructure devices. *Science* **2019**, *363*, No. eaav4450.
(36) Huang, B.; Clark, G.; Navarro-Moratalla, E.; Klein, D. R.; Cheng, R.; Seyler, K. L.; Zhong, D.; Schmidgall, E.; McGuire, M. A.; Cobden, D. H.; Yao, W.; Xiao, D.; Jarillo-Herrero, P.; Xu, X. Layer-dependent Ferromagnetism in a van der Waals Crystal down to the Monolayer Limit. *Nature* **2017**, *546*, 270−273.
(37) Gong, C.; Li, L.; Li, Z.; Ji, H.; Stern, A.; Xia, Y.; Cao, T.; Bao, W.; Wang, C.; Wang, Y.; Qiu, Z. Q.; Cava, R. J.; Louie, S. G.; Xia, J.; Zhang, X. Discovery of intrinsic ferromagnetism in two-dimensional van der Waals crystals. *Nature* **2017**, *546*, 265−269.
(38) Zheng, W.; Hong, S.; Min, B.; Wu, Y. Solution-phase synthesized iron telluride nanostructures with controllable thermally triggered p-type to n-type transition. *Nanoscale* **2018**, *10*, 20664−20670.
(39) Luxel Corporation (n.d.) Vapor Pressure Chart, https://luxel.com/wp-content/uploads/2013/04/Luxel-Vapor-Pressure-Chart.pdf (accessed 2021-02-26).
(40) Alcock, C. B. Vapor Pressure of the Metallic Elements. In *Handbook of Chemistry and Physics*, 84th ed.; Lide, D. R., Eds.; CRC Press: Boca Raton, 2003.
(41) Okamoto, H.; Tanner, L. E. The Fe-Te (Iron-Tellurium) System. *Bull. Alloy Phase Diagrams* **1990**, *11*, 371−376.
(42) Arvhult, C. M.; Poissonnet, S.; Menut, D.; Gossé, S.; Guéneau, C. Thermodynamic Assessment of the Fe-Te System. Part I: Experimental study. *J. Alloys Compd.* **2019**, *773*, 314−326.

https://doi.org/10.1021/acsomega.0c04872
ACS Omega 2021, 6, 10537−10546

(43) Ipser, H.; Komarek, K. L.; Mikler, H. Transition Metal–Chaleogen Systems, V.: The Iron–Tellurium Phase Diagram. *Monatsh. Chem.* **1974**, *105*, 1322−1334.

https://doi.org/10.1021/acsomega.0c04872
ACS Omega 2021, 6, 10537−10546